Computer-aided detection of wall motion abnormalities in cardiac MRI

Suinesiaputra, A.

7

An automated regional wall motion abnormality detection by combining rest and stress cardiac MRI: Correlation with infarct transmurality from contrast-enhanced MRI

Abstract

Objective: To evaluate the performance of an automated regional wall motion abnormality (RWMA) detection method given the combination of rest and dobutamine-induced stress cardiac MR data and to correlate the automated RWMA results with infarct transmurality assessments from contrast-enhanced MRI.
Materials and Methods: The automated RWMA method is built upon a statistical model of normokinetic myocardial contours. Forty-one rest cine-MRI of healthy volunteers were collected to build the model. Independent Component Analysis (ICA) was used to generate the probability distributions of normokinetic myocardium after several registration steps. Three normokinetic ICA models were built independently: base, mid-ventricular and apex. Twelve patients with the presence of myocardial infarction were included in the experiment. Their rest, dobutamine-induced stress and contrast-enhanced MR images in short-axis view were semi-automatically analyzed.
Results: A total of 192 myocardial segments were analyzed; 116 scar and 76 non-scar (normal) segments. For scar tissue detection, adding stress data significantly improved the performance compared to rest data only. Mean RWMA probability value differences between scar and non-scar regions with rest-stress data were wider and significant differences ($p < 0.001$, CI = 99.9%) were present in all ICA models. Combined sensitivity was 79% (base: 90%, mid: 79%, apex: 67%) and specificity was 80% (base: 83%, mid: 85%, apex: 70%). Correlated with CE-MRI, RWMA probability values decrease progressively as infarct transmurality increases.
Conclusion: Combining rest and stress MR data using automated RWMA assessment method detects scar regions more accurately than using resting MRI alone. The presented automated abnormality detector correlates well with infarct transmurality.

Submitted.

To know is to remember what you have seen.
To see is to know without remembering.

Benim Adım Kırmızı (My Name Is Red)
ORHAN PAMUK

CORONARY artery disease (CAD) has been a leading cause of death in Europe and North America and is responsible for 70% of congestive heart failure cases [1]. Although overall survival has improved, its treatment is a partial success [2, 3]. In patients with contractile reserve, where reversible myocardial dysfunction is present, treatment by coronary revascularization may lead to significant functional improvements.

In clinical practice, the assessment of dysfunctional but viable myocardium is indicated by the increase of systolic wall thickening from rest to stress. Reversible myocardial dysfunction can also be identified by contrast-enhanced MRI (CE-MRI) [4, 5]. CE-MRI allows imaging of myocardial infarction, in which scar tissues appear hyperenhanced, and the extent of infarction is the main predictor for functional outcome after revascularization. Head-to-head comparisons between rest-stress MR with infarct transmurality from CE-MRI for predicting functional improvement have been performed and they have been proven to be correlated [6–8].

During the assessment of LV functional improvement, rest and dobutamine-induced stress cine-MR images are usually compared visually. Visual wall motion scoring is prone to observer variability. Observer experience clearly affects the quality of the assessment [9]. A computer-assisted diagnosis method for the assessment of myocardial contractile reserve can be helpful to reduce the variability.

A model-based automated RWMA method has been developed in [10] and it shows good correlation with systolic wall thickening and visual wall motion score from rest MRI. This paper focuses on the improvement of the automated RWMA detection through the integration of rest and stress MR data. Evaluation is performed against scar regions (infarct transmurality) from CE-MRI.

7.1 Materials and Methods

7.1.1 Study design

Two study protocols were designed to collect control and patient groups. For the control group, forty-one healthy subjects were voluntarily enrolled in a cardiac MRI acquisition session. These subjects were part of a larger study to collect normal cardiac cine MR images from healthy population which was conducted between 2000–2004. Only short-axis view MR images were included in this study.

The patient group consisted of twelve patients suffering from chronic coronary artery disease. Each patient gave written informed consent to the study protocol that was approved by the local ethics committee. Mild to severe myocardial infarctions were present in these patients. The baseline characteristics of the patient and control groups are given

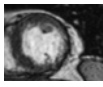

TABLE 7.1: Patient and Control Groups Statistics.[a]

	Patients	Controls
Subjects	12	41
Males/females	12/0	30/11
Ejection fraction (%)	44.85 (21.30)[b] 41.40 (17.23)[c]	67.91 (11.13)
Stroke volume (ml)	117.62 (73.87)[b] 82.44 (32.73)[c]	105.04 (32.16)

[a] All statistics are in average (standard deviation) form.
[b] Values from rest MR.
[c] Values from stress MR.

in Table 7.1. The mean ejection fraction in Table 7.1 indicates separation between the two groups.

7.1.2 Data acquisition

Acquisition of baseline MR images was performed on 1.5T Gyroscan ACS-NT MRI Scanner (Philips Medical System, Best, the Netherlands) using a 5-element synergy coil during breath-holds and were gated to the electrocardiogram. The heart was imaged from apex to base with 10 to 12 imaging levels in the short-axis orientation. Typical imaging parameters are 400×400 mm^2 field-of-view, 10 mm slice thickness, 256×256 image resolution and 1.5 mm pixel size.

Geometry settings in baseline scans were stored and repeated for low-dose dobutamine and contrast-enhanced acquisitions. The dobutamine-induced stress (DSMR) and CE-MRI acquisitions were only applied to the patient group. CE-MR images were acquired 15 minutes after a bolus injection of gadolinium diethylenetriamine pentaacetic acid (0.15 mmol/kg, Magnevist; Schering/Berlex, Berlin, Germany). Typical imaging parameters for dobutamine MRI were similar with the rest condition and also for the CE-MRI, except that the slice thickness for CE-MRI is smaller (5 mm), which gives CE-MRI more slice levels than rest MRI.

7.1.3 Slice selection

Three short-axis slice levels were visually determined in rest MRI by using particular anatomical landmarks. The basal level was defined at the short-axis slice level before the septal opening is visible. The apical level was set to the short-axis slice level where LV blood cavity is still visible in all cardiac phases. The mid-ventricular level was defined at the middle level between the basal and the apical slices. Their corresponding slice levels in DSMR and CE-MRI were automatically calculated based on 3D geometrical information obtained by using MR Analytical Software System (MASS, v5.0, Medis, Leiden, the Netherlands) [11]. Due to the smaller slice thickness of CE-MRI compared to cine-MRI, one or two CE-MR images can be associated to a slice level in cine-MRI. In case of two

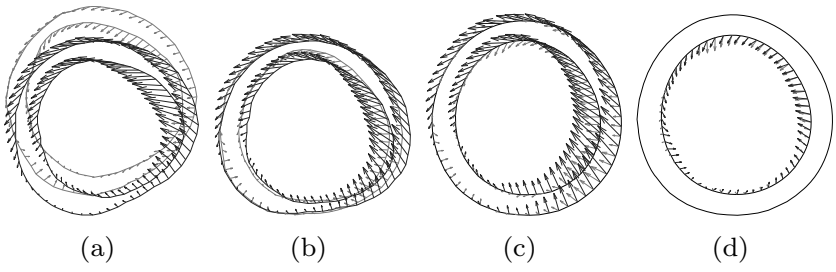

FIGURE 7.1: Patient shape results after each registration step: (a) input contours, (b) post Procrustes alignment, (c) unit contraction, and (d) post rest-stress normalization. Vectors show contraction from ED to ES. Rest and dobutamine-induced stress contraction are shown with light grey and dark grey vectors, respectively.

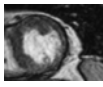

CE-MR images were selected, the analysis of infarct transmurality from these images were averaged.

7.1.4 Myocardial contour delineation and segmental definition

An expert delineated endo- and epicardial contours by using the MASS software [11]. Papillary muscles were considered as part of LV cavity and epicardial fat was excluded. Only contours at end-diastole (ED) and end-systole (ES) were taken for the automated analysis. The same software was used to delineate infarct regions on CE-MRI.

Between endo- and epicardial contours, the myocardium was divided into several segments during the validation. The 17-segment model conforming to American Heart Association [12] was applied. Only the 17th segment (the apical tip in long-axis view) was excluded in this study.

7.1.5 Normokinetic myocardial shape models

A myocardial shape was defined as a sequential concatenation of endo- and epicardial landmark points, which were taken from both end-diastole (ED) and end-systole (ES) cardiac phases. Landmark points were determined by equi-angular homologous sampling starting from the inferior intersection between right and left ventricles clockwise. A normokinetic myocardial shape is a myocardial shape from the control group. To eliminate shape variations induced by cardiac position, orientation, size and movement between individual subjects, Procrustes alignment and thin-plate spline warping methods were applied [10].

The registration method in Chapter 6 was modified to allow a proper comparison between rest and stress myocardial shapes. Additional thin-plate spline warping was performed at the last registration step to remove epicardial shape variations at ES. Without

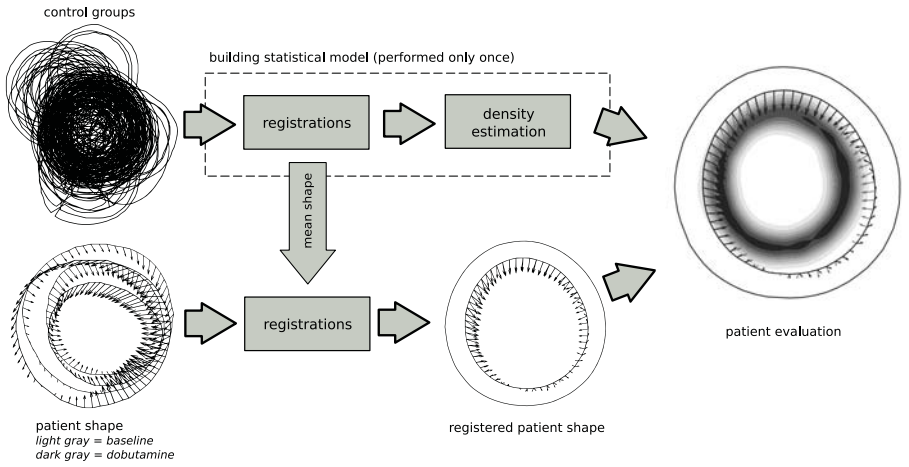

FIGURE 7.2: Schematic diagram of the automated RWMA assessment. An example of a patient with hypokinetic segment around the lateral inferior wall is presented (light gray=rest, dark gray=stress). These hypokinetic landmark points fall outside the normokinetic distributions (the black strip region in the rightmost figure).

this step, shapes induced by dobutamine stress may produce false abnormal region from epicardial contour. Epicardial landmark points at ES might fall outside the distribution of control points. An example of step-by-step registration results are shown in Figure 7.1. After the last registration step, shape variations are only present in the es-endo contour.

7.1.6 Building RWMA probability density functions

The processes of building the statistical shape model and estimating RWMA density functions were equivalent to the methods reported earlier in Chapter 6. Independent Component Analysis (ICA) was applied to decompose local shape variations. Probability density functions of control group coefficient values were constructed for each independent component. Based on the statistical independency assumption of ICA, the density functions were propagated from the independent component domain to the shape domain. This allows direct landmark point evaluation of a patient shape without projecting it first into the ICA model. The schematic diagram of the RWMA assessment is shown in Figure 7.2.

7.1.7 RWMA evaluation

RWMA evaluation was performed by aligning a patient myocardial shape with the ICA model of the control group and calculating the probability values from the aligned shape

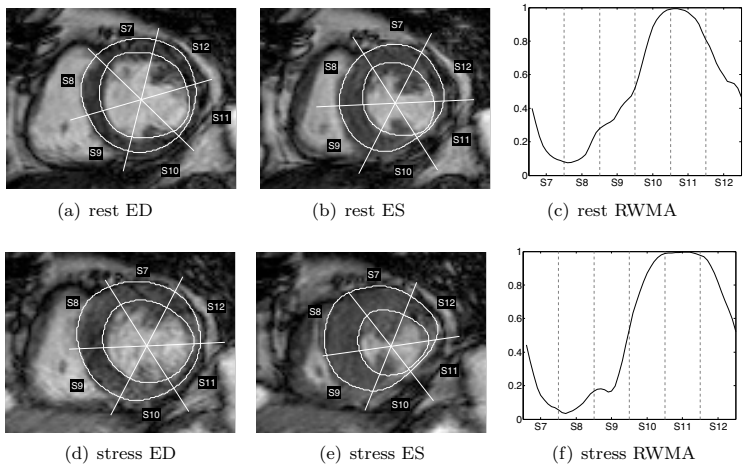

(a) rest ED (b) rest ES (c) rest RWMA

(d) stress ED (e) stress ES (f) stress RWMA

FIGURE 7.3: An example of RWMA probability values from rest (top row images) and stress (bottom row images) MR images. This example is taken from the mid-ventricular level (segments S7, S8, S9, S10, S11 and S12).

with respect to the RWMA density functions. When the RWMA probability values of two myocardial shapes from the same patient were evaluated, they will produce similar profile lines. This behavior was observed in the rest and stress shapes of the same patient (see Figure 7.3(c) and Figure 7.3(f) for an example). Hypokinetic regions that do not increase its function at stress will be visible due to the last registration step that normalizes myocardial shape at stress. In the example in Figure 7.3, non-improved hypokinetic regions are present in segment S10 and S11. These segments show small increase of RWMA probability values from rest to stress.

The combination of rest and stress data can therefore be used to detect improved and non-improved segments in terms of RWMA probability value changes. Since the ICA model was built from baseline control groups, the myocardial shape at rest can be used as the baseline to quantify the changes.

Let N be the total number of landmark points from concatenating epicardial and endocardial contours after the equi-angular sampling. Each landmark point will have its own RWMA density function, $i = 1,\ldots,N$. Let $\rho_r^{(i)}$ and $\rho_s^{(i)}$ be the RWMA probability values of the ith landmark point for rest and stress, respectively. The magnitude of RWMA probability value changes from rest to stress can be formulated as follows

$$\Delta P^{(i)} = \frac{\rho_r^{(i)} - \rho_s^{(i)}}{1 + \max\left\{\rho_r^{(i)}, \rho_s^{(i)}\right\}} \tag{7.1}$$

A negative value of $\Delta P^{(i)}$ indicates no wall motion improvement and a positive $\Delta P^{(i)}$

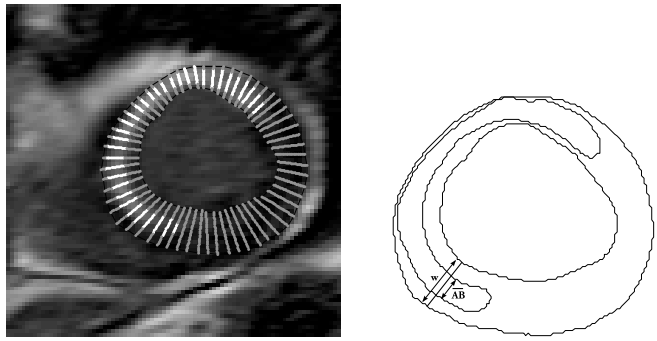

FIGURE 7.4: Transmurality chord lines. In the left figure, the white segments are the transmural extent of the chord lines (gray lines).

value shows a possible improvement of the myocardium towards normokinetic motion. The RWMA probability value changes from rest to stress is given by

$$P^{(i)} = (1 - \rho_r^{(i)}) + \Delta P^{(i)} \tag{7.2}$$

7.1.8 Transmural extent

Infarct transmurality was calculated by creating a series of chord lines (see Figure 7.4). The percentage of transmurality is defined as

$$\text{TE} = \frac{\overline{\text{AB}}}{w} \times 100\% \tag{7.3}$$

where $\overline{\text{AB}}$ is the transmural length over the chord line and w is the wall thickness.

During the experiment, TE values were averaged on each myocardial segment and graded into the following groups: absence of hyperenhancement, transmural extent of less than 25%, transmural extent of between 25%–50%, between 50%–75%, and transmural extent more than 75%.

7.1.9 Statistical analysis

Statistical shape modeling, registrations, and patient evaluation were implemented in Matlab (Matlab v7.0, The Mathworks, Natick, MA, USA). The Matlab implementation of FastICA method to generate ICA components was applied [13]. Receiver operating characteristics (ROC) graph was produced by ROCR library package (ROCR v1.0.2) [14]. The optimal cut-off value from the ROC curve is defined by minimizing $(1 - \text{sensitivity})^2 + (1 - \text{specificity})^2$. Standard sensitivity and specificity measurements were used to show the

TABLE 7.2: Segmental RWMA probability values.

segments	samples		rest only		rest-stress	
	$\mathfrak{S}'$	$\mathfrak{S}$	$\hat{P}_r \in \mathfrak{S}'$	$\hat{P}_r \in \mathfrak{S}$	$\hat{P}_s \in \mathfrak{S}'$	$\hat{P}_s \in \mathfrak{S}$
basal anterior	9	3	0.25 (0.14)	0.43 (0.15)	0.29 (0.10)	0.5 (0.23)
basal anteroseptal	11	1	0.33 (0.15)	*	0.32 (0.15)	*
basal inferoseptal	7	5	0.15 (0.12)	0.39 (0.13)	0.41 (0.16)	0.46 (0.26)
basal inferior	4	8	0.34 (0.13)	0.38 (0.13)	0.27 (0.07)	0.74 (0.20)
basal inferolateral	3	9	0.36 (0.21)	0.57 (0.18)	0.24 (0.10)	0.81 (0.15)
basal anterolateral	4	8	0.39 (0.20)	0.44 (0.12)	0.27 (0.20)	0.57 (0.26)
base	**38**	**34**	**0.30 (0.16)**	**0.46 (0.14)**	**0.30 (0.13)**	**0.62 (0.22)**
mid anterior	6	6	0.39 (0.29)	0.48 (0.07)	0.31 (0.10)	0.62 (0.20)
mid anteroseptal	5	7	0.39 (0.39)	0.53 (0.11)	0.27 (0.20)	0.71 (0.18)
mid inferoseptal	4	8	0.33 (0.16)	0.44 (0.14)	0.42 (0.22)	0.54 (0.15)
mid inferior	5	7	0.55 (0.16)	0.43 (0.19)	0.32 (0.20)	0.82 (0.12)
mid inferolateral	3	9	0.48 (0.13)	0.62 (0.18)	0.27 (0.15)	0.81 (0.17)
mid anterolateral	3	9	0.74 (0.13)	0.44 (0.17)	0.39 (0.26)	0.63 (0.16)
middle	**26**	**46**	**0.48 (0.21)**	**0.49 (0.14)**	**0.33 (0.19)**	**0.69 (0.16)**
apical anterior	5	7	0.68 (0.22)	0.66 (0.17)	0.47 (0.25)	0.82 (0.16)
apical septal	2	10	0.68 (0.09)	0.72 (0.17)	0.44 (0.24)	0.61 (0.20)
apical inferior	2	10	0.81 (0.17)	0.75 (0.15)	0.68 (0.01)	0.80 (0.13)
apical lateral	3	9	0.77 (0.05)	0.67 (0.21)	0.66 (0.10)	0.88 (0.10)
apex	**12**	**36**	**0.74 (0.13)**	**0.70 (0.17)**	**0.56 (0.15)**	**0.78 (0.15)**

$\mathfrak{S}'$ is non-scar segments and $\mathfrak{S}$ is scar segments. $\hat{P}_r \in \mathfrak{S}'$ and $\hat{P}_r \in \mathfrak{S}$ are the mean RWMA probability values at rest for non-scar and scar segments, respectively. $\hat{P}_s \in \mathfrak{S}'$ and $\hat{P}_s \in \mathfrak{S}$ are the mean RWMA probability values at stress for non-scar and scar segments, respectively. All values are in mean (standard deviation) format. The symbol $*$ indicates non-available statistical data because the number of samples for that particular case is not enough. Segments are labeled as defined by American Heart Association standardization for myocardial segments [12].

method's performance [15]. The significant differences of RWMA probability values between scar and non-scar segments were tested by unpaired two-tailed t-tests with 99.9% confidence interval. P-values < 0.001 were considered significant.

7.2 Results

7.2.1 Rest versus rest-stress data

Two evaluations for scar tissue detection were compared: RWMA probability values from rest MRI only and RWMA probability values from the combination of rest and stress MRI. A scar tissue is a region where transmural extent exceeds 1%. The results are shown in Table 7.2.

The mean differences between scar and non-scar segments for rest-stress data in Table 7.2 are significantly larger than for rest data only. This indicates a better separation of scar tissues by the combination of rest and stress data. The unpaired t-tests resulted in significant differences of mean RWMA probability values between scar and non-scar

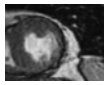

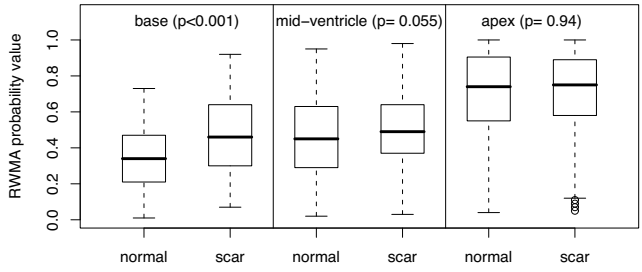

(a) rest only

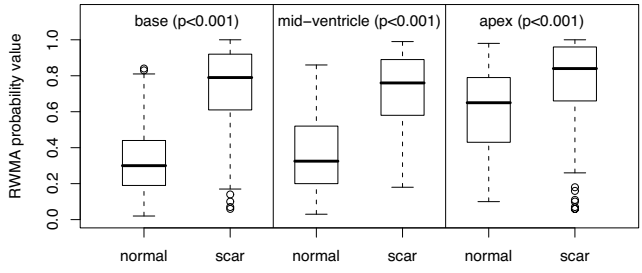

(b) rest-stress

FIGURE 7.5: Distributions of RWMA probability values from scar and non-scar (normal) segments for each slice model, presented by box-and-whisker plots. Unpaired t-tests were performed with 99% confidence level to get the p-values.

segments in all three slice levels ($p < 0.001$ for base, mid-ventricular and apex) when rest and stress data were combined. If only rest data were used, then only the basal model showed significant difference ($p < 0.001$); the mid-ventricular model resulted $p = 0.06$ and apical model was $p = 0.94$. These findings are graphically presented by box plots in Figure 7.5. Based on this observation, the remaining experimental studies in this paper used only the combination of rest and stress data.

7.2.2 Scar tissue detection

Receiver operating characteristics (ROC) curve to detect scar tissue by using rest and stress data is given in Figure 7.6. The area under the ROC curve was 0.88. Sensitivity and specificity of the method were 79% and 80%, respectively. These were combined from basal, mid-ventricular and apical models. The sensitivity values for each model were 90% (base), 79% (mid-ventricular) and 67% (apex), while for specificity values were 83% (base), 85% (mid-ventricular) and 70% (apex).

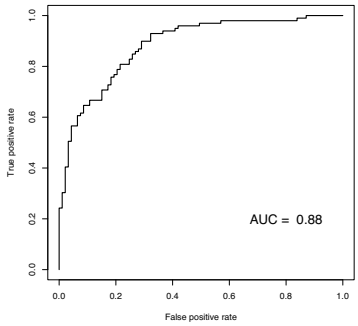

FIGURE 7.6: ROC curve of the method performance to detect hyperenhanced segments.

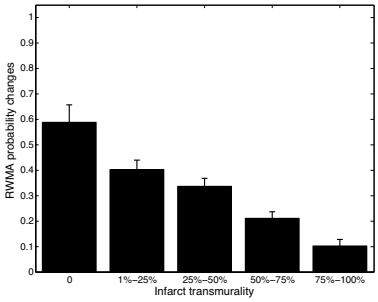

FIGURE 7.7: Distributions of RWMA probability values grouped by infarct transmuralities. Error bars indicate standard error values.

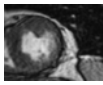

7.2.3 Correlation with infarct transmurality

From the total of 192 segments, 116 (60.4%) segments showed hyperenhancement. Out of these scar segments, 32 (16.7%) segments had less than 25% transmurality, 40 (20.8%) segments with 25%–50% transmurality and 32 (16.7%) segments with 50%–75% transmurality. Severe infarct transmurality of over 75% was observed in 12 (6.2%) segments.

Distributions of RWMA probability values over each of the scarring score groups are shown in Figure 7.7. It shows that the RWMA probability values decrease progressively as infarct transmurality increases. There is a clear separation between transmural and non-transmural regions. This shows that the automated rest-stress RWMA assessment method correlates well with the infarct transmurality from CE-MRI. A visual example of this finding is illustrated in Figure 7.8.

7.3 Discussion

Two main objectives were addressed in this chapter: (1) to evaluate the performance of the automated RWMA detection method when stress and rest data are combined, and (2) to correlate the RWMA probability changes estimated from the automated method with infarct transmurality from CE-MR images. From the result section, the RWMA probability values from the combined rest and stress data has proven to produce a significant improvement in distinguishing scar regions compared to the use of rest data only. The separation between scar and non-scar regions widened considerably when stress data was included.

On the detection of scar regions, the performance of the automated method with the combination of rest and stress data was relatively high. The area under RWMA probability

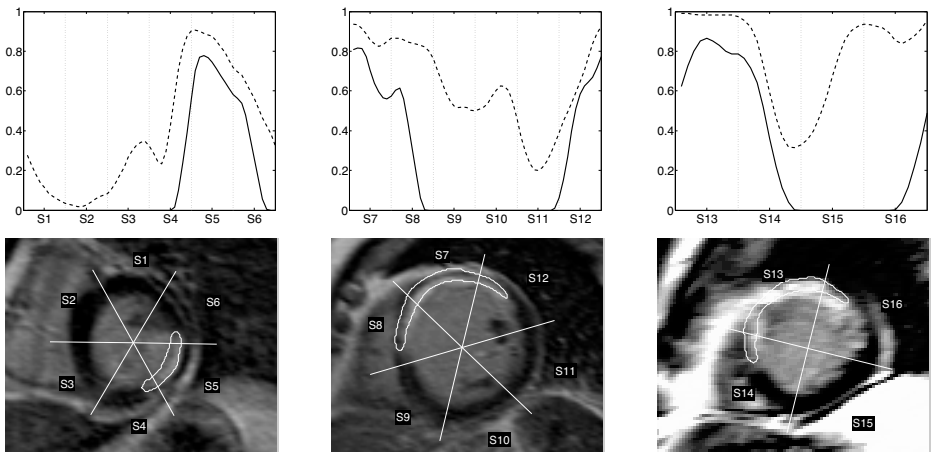

(a) base (b) mid-ventricular (c) apex

FIGURE 7.8: Visual comparisons of RWMA profile lines (top rows) and their corresponding CE-MR images (bottom rows). In the profile lines, solid lines are infarct transmurality and the dashed lines are the RWMA probability values from rest to stress.

value curve was 0.88 (see Figure 7.6), which proves the method's capability to detect scar regions. Significant differences of mean RWMA probability values between scar and non-scar regions were demonstrated in all models.

Correlated with the infarct transmurality, the automated detection method produced decreasing RWMA probability values as the transmural extent increases. In Kim et. al. [4] the likelihood of improvement in dysfunctional segments after revascularization increases when the transmural extent decreases. This means that the estimated RWMA probability values may explain the same likelihood of contractile reserve.

Currently, myocardial contours for both control and patient groups, including the hyperenhanced boundaries, were drawn manually by an expert. This experimental study was conducted to demonstrate the proof of concept of the automated RWMA assessment for the rest and stress data. However, providing manual contours is prone to subjectivity and a tedious task. Especially for the apical regions, drawing endocardial borders is problematic because of the low contrast at the later systolic phases. Endocardial borders were sometimes almost invisible at end-systole. As a result, the apical model yielded the lowest score in detecting scar regions (67% sensitivity and 70% specificity) compared to basal and mid-ventrical models. This raises the necessity to apply an objective segmentation method for myocardium. Statistical-based segmentation methods that incorporate temporal information, e.g. [16–18], can be applied in this case to solve this problem.

The main limitation of this study is the lack of follow up data after revascularization to assess functional recovery completely. The current validation used infarct transmu-

rality as the ground truth, but CE-MRI also possesses significant problems for viability assessment [19]. Therefore this study does not evaluate the method's capability to assess myocardial viability, but the proposed method shows good correlation with infarct transmurality. Additional pre- and post-treatment patient data is needed to further explore the capability of the proposed method to quantify regional LV functional improvement.

The current statistical model is trained from ED and ES phases only. The results show that building the statistical model from these two phases is enough to capture the kinetics of heart motion. However, a higher temporal resolution may improve the performance of the method, but at the expense of more contour drawing.

In conclusion, we have presented an automatic quantification method of RWMA analysis that combines information from resting and stress MR. Validated against CE-MRI, the automated method behaves as expected, i.e., it decreases when transmural extent increases. Hence, the proposed method correlates well with CE-MRI and therefore is a promising diagnostic tool to automatically assess RWMA from cardiac MR images.

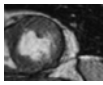

7.4 References

[1] H. Mahrholdt, I. Klem, and U. Sechtem, "Cardiovascular MRI for detection of myocardial viability and ischaemia," *Heart*, vol. 93, no. 1, pp. 122–129, 2007.

[2] T. E. Owan, D. O. Hodge, R. M. Herges, S. J. Jacobsen, V. L. Roger, and M. M. Redfield, "Trends in prevalence and outcome of heart failure with preserved ejection fraction," *N Engl J Med*, vol. 355, no. 3, pp. 251–259, Jul 2006.

[3] P. G. Camici, S. K. Prasad, and O. E. Rimoldi, "Stunning, hibernation, and assessment of myocardial viability," *Circulation*, vol. 117, no. 1, pp. 103–114, Jan 2008.

[4] R. J. Kim, E. Wu, A. Rafael, E. L. Chen, M. A. Parker, O. Simonetti, F. J. Klocke, R. O. Bonow, and R. M. Judd, "The use of contrast-enhanced magnetic resonance imaging to identify reversible myocardial dysfunction," *N Engl J Med*, vol. 343, no. 20, pp. 1445–1453, Nov 2000.

[5] A. Saraste, S. Nekolla, and M. Schwaiger, "Contrast-enhanced magnetic resonance imaging in the assessment of myocardial infarction and viability," *J Nucl Cardiol*, vol. 15, no. 1, pp. 105–117, Jan-Feb 2008.

[6] M. Gutberlet, M. Frohlich, S. Mehl, H. Amthauer, H. Hausmann, R. Meyer, H. Siniawski, J. Ruf, M. Plotkin, T. Denecke, B. Schnackenburg, R. Hetzer, and R. Felix, "Myocardial viability assessment in patients with highly impaired left ventricular function: Comparison of delayed enhancement, dobutamine stress MRI, end-diastolic wall thickness, and TI201-SPECT with functional recovery after revascularization," *Eur Radiol*, vol. 15, no. 5, pp. 872–880, May 2005.

[7] T. A. M. Kaandorp, J. J. Bax, J. D. Schuijf, E. P. Viergever, E. E. van Der Wall, A. de Roos, and H. J. Lamb, "Head-to-head comparison between contrast-enhanced magnetic resonance imaging and dobutamine magnetic resonance imaging in men with ischemic cardiomyopathy," *Am J Cardiol*, vol. 93, no. 12, pp. 1461–4, Jun 2004.

[8] E. Wellnhofer, A. Olariu, C. Klein, M. Grafe, A. Wahl, E. Fleck, and E. Nagel, "Magnetic resonance low-dose dobutamine test is superior to SCAR quantification for the prediction of functional recovery," *Circulation*, vol. 109, no. 18, pp. 2172–2174, May 2004.

[9] I. Paetsch, C. Jahnke, V. A. Ferrari, F. E. Rademakers, P. A. Pellikka, W. G. Hundley, D. Poldermans, J. J. Bax, K. Wegscheider, E. Fleck, and E. Nagel, "Determination of interobserver variability for identifying inducible left ventricular wall motion abnormalities during dobutamine stress magnetic resonance imaging," *Eur Heart J*, vol. 27, no. 12, pp. 1459–1464, Jun 2006.

[10] A. Suinesiaputra, A. F. Frangi, T. A. M. Kaandorp, H. J. Lamb, J. J. Bax, J. H. C. Reiber, and B. P. F. Lelieveldt, "Automated detection of regional wall motion abnormalities based on a statistical model applied to multislice short-axis cardiac MR images," *IEEE Trans Med Imaging*, vol. 28, no. 4, pp. 595–607, Apr 2009.

[11] R. J. van der Geest, V. G. Buller, E. Jansen, H. J. Lamb, L. H. Baur, E. E. van der Wall, A. de Roos, and J. H. Reiber, "Comparison between manual and semiautomated analysis of left ventricular volume parameters from short-axis MR images," *J Comput Assist Tomogr*, vol. 21, no. 5, pp. 756–765, Sep-Oct 1997.

[12] M. D. Cerqueira, N. J. Weissman, V. Dilsizian, A. K. Jacobs, S. Kaul, W. K. Laskey, D. J. Pennell, J. A. Rumberger, T. Ryan, and M. S. Verani, "Standardized myocardial segmentation and nomenclature for tomographic imaging of the heart: a statement for healthcare professionals from the Cardiac Imaging Committee of the Council on Clinical Cardiology of the American Heart Association," *Circulation*, vol. 105, no. 4, pp. 539–542, 2002.

[13] A. Hyvärinen and E. Oja, "Independent component analysis: algorithms and applications," *Neural Networks*, vol. 13, pp. 411–430, June 2000.

[14] T. Sing, O. Sander, N. Beerenwinkel, and T. Lengauer, "ROCR: visualizing classifier performance in R," *Bioinformatics*, vol. 21, no. 20, pp. 3940–3941, 2005.

[15] T. A. Lasko, J. G. Bhagwat, K. H. Zou, and L. Ohno-Machado, "The use of receiver operating characteristic curves in biomedical informatics," *J Biomed Inform*, vol. 38, no. 5, pp. 404–415, 2005.

[16] A. Andreopoulos and J. K. Tsotsos, "Efficient and generalizable statistical models of shape and appearance for analysis of cardiac MRI," *Medical Image Analysis*, vol. 12, no. 3, pp. 335–357, JUN 2008.

[17] R. Lapp, M. Lorenzo-Valdes, and D. Rueckert, "3D/4D cardiac segmentation using active appearance models, non-rigid registration, and the insight toolkit," in *Medical Image Computing and Computer-Assisted Intervention - MICCAI 2004, Part 1, Proceedings*, ser. Lecture Notes in Computer Science, C. Barillot, D. Haynor, and P. Hellier, Eds., vol. 3216. Springer, 2004, pp. 419–426.

[18] S. C. Mitchell, J. G. Bosch, B. P. F. Lelieveldt, R. J. van der Geest, J. H. C. Reiber, and M. Sonka, "3-D active appearance models: segmentation of cardiac MR and ultrasound images," *IEEE Trans Med Imaging*, vol. 21, no. 9, pp. 1167–1178, Sep 2002.

[19] S. D. Roes, T. A. M. Kaandorp, N. A. Marsan, J. J. M. Westenberg, P. Dibbets-Schneider, M. P. Stokkel, H. J. Lamb, E. E. van der Wall, A. de Roos, and J. J. Bax, "Agreement and disagreement between contrast-enhanced magnetic resonance imaging and nuclear imaging for assessment of myocardial viability," *Eur J Nucl Med Mol Imaging*, vol. 36, no. 4, pp. 594–601, Apr 2009.